Journal of Solid State Chemistry **163,** 498–505 (2002)
doi:10.1006/jssc.2001.9437, available online at http://www.idealibrary.com on IDEAL®

Synthesis, Magnetic and Electronic Properties of Single Crystals of $EuMn_2P_2$

Amy C. Payne, Angella E. Sprauve, Marilyn M. Olmstead, and Susan M. Kauzlarich[1]

Department of Chemistry, University of California, One Shields Avenue, Davis, California 95616, USA

and

Julia Y. Chan,[2] B. A. Reisner,[3] and J. W. Lynn[1]

NIST Center for Neutron Research, National Institute of Standards and Technology, Gaithersburg, Maryland 20899-8562

Received July 2, 2001; in revised form October 8, 2001; accepted October 26, 2001

Large single crystals of $EuMn_2P_2$ were grown from a tin flux whose melt composition and reaction temperature profile were optimized to avoid impurity phases. The crystal structure of $EuMn_2P_2$ is of the $CaAl_2Si_2$ structure type. The structure was determined by single-crystal X-ray crystallography, with the unit cell in the trigonal lattice, $a = 4.1294(3)$ Å and $c = 6.9936(8)$ Å, at $T = 90$ K ($Z = 1$, $R1 = 0.0239$, w$R2 = 0.0632$) and belongs to the $P\bar{3}m1$ ($\#164$) space group. Temperature-dependent magnetic susceptibility, resistivity, and neutron diffraction measurements on single crystals indicate that $EuMn_2P_2$ is an antiferromagnetic insulator with a Neél temperature of 16.5 ± 0.25 K. The Eu spins order in a simple magnetic structure where the spins in the *a–b* plane are aligned ferromagnetically; these ferromagnetic planes are stacked antiferromagnetically along the *c*-axis.

INTRODUCTION

A well-known synthetic technique for the preparation of solid state compounds is precipitation or growth from a molten metal flux (1–6). Flux growth has been employed for the synthesis of a variety of materials (2, 3, 7) since the use of a flux allows for compounds previously known only by traditional high-temperature routes to be synthesized at lower temperatures. The metal flux method is useful for exploratory synthesis because well-formed single crystals can be grown for structure and property measurements when the appropriate reaction conditions are used. One variation on this technique is to dissolve the pure elements of a target compound in a molten metal that is chosen for its relatively low melting point ($< 900°C$) and inertness to the reactants and the reaction vessel. While the flux properties determine the success of the reaction to some degree, optimization of the reactions conditions (i.e., temperature, stoichiometry) allows for control over unwanted flux interactions. The appropriate crystal growing conditions are not always found for the target compound due to the complex phase equilibria occurring in multicomponent melts. However, this complexity can lead to the discovery of new compounds (8–13), or, in this case, new routes to the preparation of known compounds.

Single crystals of the $EuMn_2P_2$ phase were discovered as a byproduct from a Sn flux while trying to grow large single crystals of $Eu_{14}MnP_{11}$ for magnetoresistance measurements (14). $EuMn_2P_2$ (15) has been synthesized and characterized previously by powder X-ray diffraction and is isostructural with $SrMn_2P_2$ ($CaAl_2Si_2$ structure type) (16): however, no single crystals were obtained or property measurements performed. Single-crystal X-ray diffraction, temperature-dependent magnetization, temperature-dependent resistivity, and powder neutron diffraction data have been reported for $SrMn_2P_2$ (17, 18). Powder neutron diffraction data confirmed antiferromagnetic ordering of the Mn^{2+} moments and showed that there are two sets of magnetic reflections with different temperature dependencies (18). However, two-dimensional magnetic frustration is expected within the $[Mn_2P_2]^{2-}$ sheets, as well as between the sheets in the third dimension due to the trigonal symmetry of the structure, making a complete magnetic structure difficult to determine. The growth of large single crystals of $EuMn_2P_2$ presents an opportunity to revisit this study by gathering more detailed information about the magnetic structure.

[1]To whom correspondence should be addressed.
[2]Present address: Department of Chemistry, Louisiana State University, Baton Rouge, LA 70803-1804.
[3]Present address: Department of Chemistry, James Madison University, Harrisonburg, VA 22807.

0022-4596/02 $35.00

This paper presents a new synthetic route to $EuMn_2P_2$. Single-crystal X-ray diffraction data, temperature-dependent magnetic susceptibility, resistivity measurements, and single-crystal neutron diffraction data for $EuMn_2P_2$ are presented and discussed.

EXPERIMENTAL

Synthesis. Crystals were initially grown from a Sn flux with the elements Eu:Mn:P:Sn in the ratio of 14:4:11:265. The title compound is grown under very dilute conditions. Large (~ 2 mm diameter), well-faceted, hexagonal single crystals of $EuMn_2P_2$ were formed by reacting the elements in a Sn flux. All reactants and products were handled under an inert (N_2) atmosphere: Eu (99.999%, Ames Lab) in 1/8″ ribbon form was cut into small pieces; Mn pieces (Alfa-Aesar, Puratronic, 99.98%) and red P (Alfa-Aesar, Puratronic, 99.9999 + %) were ground to powders with a stainless steel mortar and pestle. The elements were packed between granular Sn (Fisher Scientific, certified) in an alumina crucible; a second crucible containing quartz wool was inverted over the reaction crucible, and the entire reaction was sealed in an acid-etched fused silica jacket back-filled with 0.2 atm Ar. The tubes were flattened at one end to allow for upright placement in a furnace. Initial syntheses followed the reaction sequence: ramp to 500°C and dwell for 1 h, ramp to 1050°C and dwell for 6 h, slow cool 3°C/h to 700°C, and dwell at 700°C until the reaction vessel was removed from the furnace. In subsequent experiments, reaction vessels were removed from a muffle furnace at temperatures between 700°C and 900°C, inverted, and centrifuged to separate the crystals from the flux. The synthesis was optimized using several parameters: the flux to reactant ratio, the initial dwell temperature, the cooling rate, the final dwell temperature, and the length of the final dwell.

TABLE 1
Products Resulting from Temperature- and Concentration-Dependent Studies of 14Eu:4Mn:11P in Sn Flux

Reaction	% Sn flux[a]	Dwell temp/°C	Spin temp/°C	Product
1	90	900	~ 750	Large crystal of EuSnP
2	90	1000	~ 800	Large plates of EuSnP
3	90	1050	~ 750	EuSnP; $EuMn_2P_2$
4	90	1100	~ 800	EuSnP; $EuMn_2P_2$
5	70	1050	~ 700	EuSnP
6	80	1050	~ 700	EuSnP
7	90	1050	~ 700	EuSnP; $EuMn_2P_2$
8	93	1100	~ 800	Well-defined, faceted $EuMn_2P_2$;small amount of EuSnP
9	95	1050	~ 700	EuSnP; $EuMn_2P_2$

[a] The percentage of Sn was calculated from the ratio of Sn flux to the sum of the atomic ratios of all the elements (i.e., $265/294 \times 100\% = 90\%$).

Table 1 provides the various reaction conditions. All products were initially examined in a nitrogen-filled glove box. However, $EuMn_2P_2$ is air stable and was subsequently handled in air. There was no noticeable degradation of the sample, as determined by color or X-ray powder diffraction.

X-ray powder diffraction. The products were ground to a powder with an agate mortar and pestle and placed between pieces of cellophane tape with ca. 10% NBS SRM 640 silicon standard. The sample was transferred from the drybox to an Enraf-Nonius Guinier camera (Cu$K\alpha_1$ radiation) where the sample remained under vacuum for the duration of the data collection. Film data from samples were compared to powder patterns calculated from the single-crystal data of the title compounds as well as other known binary and ternary compounds. Digitized diffraction data were collected using a Siemens D500 diffractometer (Cu source) and an Inel diffractometer (Cu source) with a curved ion-chamber detector. Powder diffraction patterns were indexed using the calculated room temperature lattice parameters (19).

Single-crystal X-ray diffraction. Highly reflective single crystals were separated from the bulk of the sample in a dry box equipped with a microscope. Isolated, platelet single crystals as well as multifaceted crystals were present. Both morphologies appear to be $EuMn_2P_2$. The crystals were placed in Exxon Paratone-N oil. A 0.38 mm × 0.18 mm × 0.10 mm crystal was mounted on a quartz fiber attached to a copper pin with solder. The pin was mounted on the goniometer of a Bruker SMART 1000 (Mo$K\alpha$ radiation, $\lambda = 0.71073$ Å; CCD detector) with a modified Enraf-Nonius low-temperature apparatus. Absorption was corrected by an empirical method based on data redundancy (20). The structures were refined by the full-matrix least-squares method on F^2 (21) using the atomic coordinates of $SrMn_2P_2$, and the data were corrected for extinction and refined with anisotropic thermal parameters.

Single-crystal neutron diffraction. The neutron diffraction measurements were carried out at the BT-4 triple-axis spectrometer at the NIST Center for Neutron Research. A Cu(220) monochromator was employed at a neutron wavelength of 1.54 Å to reduce the effects of the absorption of Eu. The collimation before and after the monochromator was 60′–40′ full width at half-maximum (FWHM), respectively. Data were collected both with collimation after the sample and with an open detector, without an analyzer, and the integrated intensities were obtained by the θ:2θ method or the crystal rotation method, respectively. The crystal was a plate approximately 3 mm on a side and 0.7 mm thick, with the *c*-axis perpendicular to the plate. The crystal was mounted in the [*hhl*] scattering plane in a pumped helium dewar with a low-temperature capability of 1.4 K.

Experimental uncertainties indicated in this work represent one statistical standard deviation, except when noted otherwise.

Magnetic susceptibility measurements. A Quantum Design MPMS Superconducting Quantum Interference Device (SQUID) magnetometer with a 7-T superconducting magnet was used to measure dc magnetization. A quartz tube designed to have a uniform background was loaded with ~ 6 mg of single crystals; the quartz tube was then evacuated and sealed to protect the sample from decomposition. Samples for individual single crystals were prepared with a drinking straw and Apiezon-N grease. Data were collected and analyzed with Magnetic Properties Measurement System (MPMS) software provided by Quantum Design. $M(H)$ data were collected for bulk samples below and above the magnetic transition. Zero-field-cooled (ZFC; 2–300 K) and field-cooled (FC; 300–2 K) data were collected on bulk samples ($H_{\text{applied}} = H_a = 1000$ Oe) and single crystals ($H_a = 5000$ Oe).

Resistivity. The measurements were performed on a single crystal of $EuMn_2P_2$ using the four-probe method. Pt wires were attached to the crystal with Dupont silver paint. A current of 1 mA was applied across the two outer Pt leads (0.002 mil) using a Keithley 224 programmable current source, while a Keithley 671 electrometer was used to measure the potential between the inner Pt leads (0.001 mil). The temperature was controlled by a Lakeshore 91C and a Leybold CT1 Model 22 cryogenics (He closed-cycle) refrigerator. The lattice parameters of the crystal were confirmed by single-crystal X-ray crystallography.

RESULTS AND DISCUSSION

The results obtained for temperature- and concentration-dependent crystal growth studies of 14Eu:4Mn:11P in Sn flux are shown in Table 1. Crystals were initially grown from a Sn flux with the elements Eu:Mn:P:Sn in the ratio of 14:4:11:265. Synthesis optimization was performed by varying the flux to reactant ratio, the reactant composition, the cooling rate, and the spin temperature (the temperature at which the reaction was removed from the furnace and centrifuged). Two major conclusions may be drawn from this work: higher dwell temperatures favored the formation of the $EuMn_2P_2$ phase and the $EuMn_2P_2$ phase was preferred in more dilute reaction conditions (i.e., greater % Sn). Slowing the cooling rate from 3°C/h to 1°C/h resulted in the growth of larger crystals. A high spin temperature is important as well; higher spin temperatures allow the Sn flux to be removed from the product before EuSnP (22) can precipitate.

The crystallographic details for the single-crystal structure solution of $EuMn_2P_2$ are listed in Table 2. Room temperature lattice parameters of polycrystalline $EuMn_2P_2$ obtained from powder X-ray diffraction data, $a = 4.143(1)$ Å, $c = 7.034(2)$ Å, are in good agreement with those measured in the single-crystal experiment. This compound crystallizes in the $P\bar{3}m1$ space group and is isotypic with $CaAl_2Si_2$ (15). Positional parameters, anisotropic thermal parameters, and interatomic distances obtained from the single-crystal structure of $EuMn_2P_2$ are listed in Tables 3, 4, and 5, respectively. Compounds with the general formula AMn_2P_2 crystallize with either the $CaAl_2Si_2$ structure type (A = Ca, Sr, Eu) or the $ThCr_2Si_2$ structure type (A = Ba) (16). The $CaAl_2Si_2$ type is rare and is generally restricted to a particular valence electron count of 16 valence electrons per formula unit (23–27). While the electronic structure of $CaAl_2Si_2$ has been compared with the $ThCr_2Si_2$ structure (28–31), within this particular series, the contributions of the cation charge and size to the lattice energy probably determine the structure that the compound adopts (18). $EuMn_2P_2$ and $SrMn_2P_2$ are isostructural and can be

TABLE 2
Crystal Data and Structure Refinement for $EuMn_2P_2$, $P\bar{3}m1$ (164), $Z = 1$

Formula weight/g mol^{-1}	323.78
Temperature/K	298(2)
Unit cell dimensions/Å	$a = 4.1294(3)$ $c = 6.9936(8)$
Volume (Å^3)	103.28(2)
Density (calculated) (g/cm^3)	5.206
μ Mo$K\alpha$ (mm^{-1})	21.554
θ range	2.91 to 31.43°
Reflections collected	7871
Independent reflections	159 [R(int) = 0.0576]
Observed reflections ($I > 2\sigma(I)$)	159
Max. and min. transmission	0.2218 and 0.0448
Data/restraints/parameters	159/0/10
S (Goodness-of-fit on F^2)	1.233
R indices (all data)[a,b]	$R1 = 0.0239$, w$R2 = 0.0632$
Extinction coefficient	0.23(2)
Largest diff. peak and hole/e Å^{-3}	1.723 and -1.764

[a] $R_1 = \sum||F_o| - |F_c||/\sum|F_o|$.
[b] $wR_2 = [\sum[w(F_o^2 - F_c^2)^2]/\sum[w(F_o^2)^2]]^{1/2}$, $w^{-1} = [\sigma^2(F_o^2) + (0.0305p)^2 + 28.39]$, where $p = [\max(F_o^2,0) + 2F_c^2]/3$.

TABLE 3
Atomic Coordinates and Equivalent Isotropic Displacement Parameters (Å^2) for $EuMn_2P_2$[a]

		x	y	z	U(eq)
Eu	$1a\bar{3}m$	0	0	0	0.003(1)
Mn	$2d3m$	0.3333	-0.3333	0.3791(2)	0.003(1)
P	$2d3m$	0.3333	-0.3333	0.7309(3)	0.004(1)

[a] U(eq) is defined as one-third of the trace of the orthogonalized U_{ij} tensor. There is one formula unit in the chemical unit cell, with the Eu at the origin and the two Mn and P at $\pm z$.

TABLE 4
Anisotropic Displacement Parameters ($Å^2 \times 10^3$) for $EuMn_2P_2$

	U_{11}	U_{22}	U_{33}	U_{23}	U_{13}	U_{12}
Eu	4(1)	4(1)	1(1)	0	0	2(1)
Mn	5(1)	5(1)	1(1)	0	0	2(1)
P	5(1)	5(1)	2(1)	0	0	2(1)

[a] The anisotropic displacement factor exponent takes the form $-2\pi^2[h^2a^{*2}U_{11} + \cdots + 2hka^*b^*U_{12}]$.

rationalized by the Zintl concept: the cations, Eu^{2+} or Sr^{2+}, donate valence electrons to form two-dimensional $[Mn_2P_2]^{2-}$ layers. The two-dimensional $[Mn_2P_2]^{2-}$ layers alternate with planes of A^{2+} cations stacked along [001] as shown in Fig. 1.

Figure 2 shows a stereoview of the unit cell down the *c*-axis. The coordination of the Mn^{2+} is tetrahedral by P^{3-} while the PMn_4 unit has an umbrella-shaped geometry. A theoretical study of site preferences of the $CaAl_2Si_2$ type shows that the more electronegative element prefers the umbrella site, while the tetrahedral site is occupied by the more electropositive element of the anionic network (30): $EuMn_2P_2$ fits this model. Main group compounds with the $CaAl_2Si_2$, or more generally the AB_2X_2 structure, are composed of two different B–X bond distances, which are defined with respect to the umbrella site; there are three equivalent "rib" bonds and one "handle" bond (30). According to calculations this difference is minimized when B is an ion with a half-filled *d*-shell (e.g., Mn^{2+}). This theoretical result is in agreement with previous empirical results as well as the Mn–P bond distances (2.460 Å Mn–P handle, 2.5051 Å; rib) presented in this paper.

The bulk magnetic susceptibility of $EuMn_2P_2$ is shown in Fig. 3. The sample displays paramagnetic behavior at higher temperatures and undergoes an antiferromagnetic transition at 18 K. The paramagnetic data (50–300 K) were fit by a modified Curie–Weiss law ($\chi = C/(T - \theta + \chi_0)$) to obtain the following parameters: $\chi_0 = 0.0041(5)$ emu/mol, $C = 7.75(8)$; and $\theta = 12.1(4)$ K). The fit results in an effective

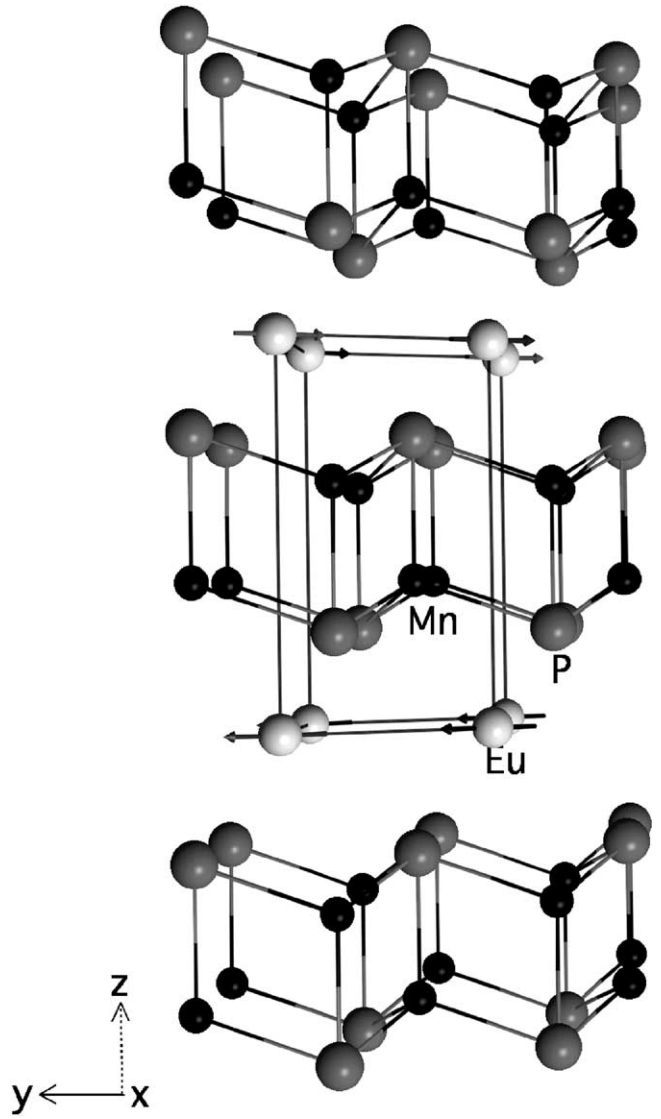

FIG. 1. The stacked $[Mn_2P_2]^{2-}$ layers and cation planes of $EuMn_2P_2$ as viewed along [100]. The magnetic structure consists of spins in the *a*–*b* plane that are coupled ferromagnetically within the plane and stacked antiferromagnetically along the *c*-axis.

TABLE 5
Bond Lengths (Å) and Angles (°) for $EuMn_2P_2$

Eu–P	3.038(1)
Eu–Mn	3.566(1)
Mn–P "handle"	2.460(3)
Mn–P "rib"	2.5051(8)
Mn–Mn	2.923(2)
P–Mn–P	107.88(6)
P–Mn–P	111.01(5)
Mn–Mn–Mn	89.89(6)
Mn–P–Mn	72.12(6)
P–Mn–P	111.01(5)

moment of 7.87 μ_B per $EuMn_2P_2$ formula unit. This is in good agreement with the expected spin-only value for $Eu^{2+}(f^7)$ of 7.94 μ_B, but much lower than the moment expected for both Mn^{2+} and Eu^{2+} (11.52 μ_B). Hysteresis loops are linear at 5 K, indicating no net ferromagnetic component to the ordering in the sample. This susceptibility is similar to the magnetic susceptibility of $EuAl_2Si_2$ and $EuAl_2Ge_2$ which are isostructural but metallic (27).

Figure 4 shows the temperature-dependent magnetic susceptibility data for a single crystal of $EuMn_2P_2$ with the *c*-axis oriented perpendicular to the applied magnetic field. As in the bulk sample, an antiferromagnetic transition occurs at 18 K. Below about 15 K, the magnetism is linear, as

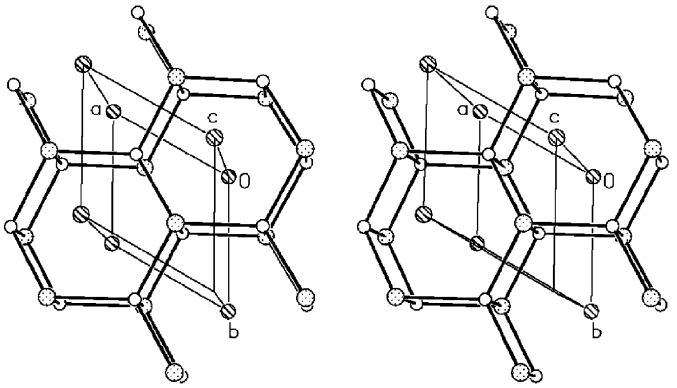

FIG. 2. A stereoview showing the coordination around the Mn and P atoms. Mn and P are represented by open and filled circles, respectively. Eu atoms are at the corners of the unit cell.

expected for an antiferromagnet with the easy axis perpendicular to the applied field. The surface of the crystal is wetted with an alloy of Sn, possibly Eu–Sn or Mn–Sn based, despite attempts made to clean the crystal with different concentrations of HCl (*aq*). The lack of a superconducting transition at 4 K in any of the susceptibility measurements indicates that the substance wetting the crystal surface is not likely to be pure Sn ($T_c = 4.2$ K).

Of the two magnetic ions, $Eu^{2+}(f^7)$ and $Mn^{2+}(d^5)$, ordering of Eu^{2+} is expected to produce the antiferromagnetic ordering observed at 18 K. This interpretation is supported by the temperature-dependent magnetic susceptibility and neutron data of $SrMn_2P_2$ published previously, where the Mn spin order above room temperature (18). Sr^{2+} and

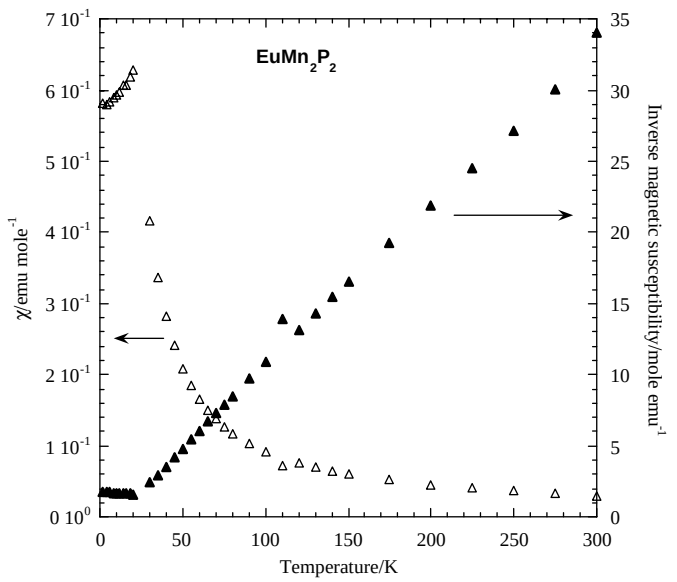

FIG. 3. Bulk magnetic susceptibility and inverse susceptibility as a function of temperature for $EuMn_2P_2$ at $H_a = 0.1$ T.

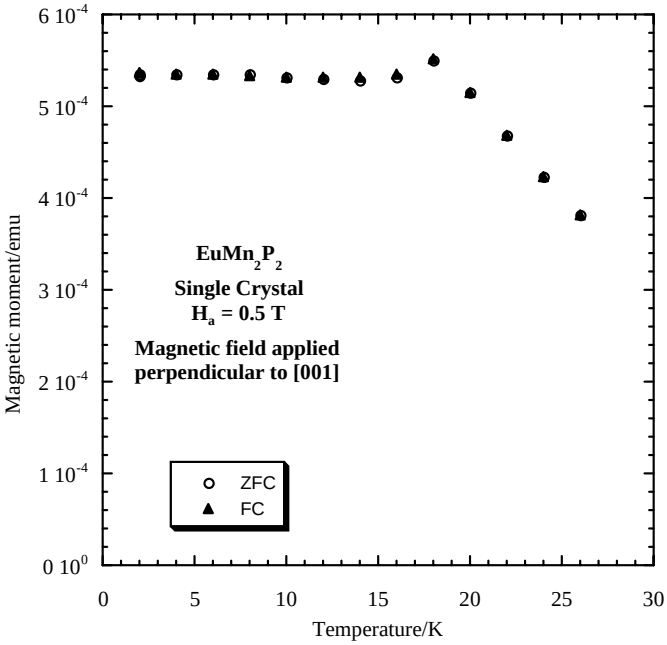

FIG. 4. Low-temperature magnetic moment of a single crystal with the magnetic field applied perpendicular to [001] ($H_a = 0.5$ T).

Eu^{2+} have similar atomic radii which limits the effect of steric or structural differences, such as the effect of bond angles in the anionic portion of the structure and the distance between anionic layers, on the magnetic behavior. Therefore, it is possible to focus on the differences in magnetic behavior arising from magnetic exchange interactions. When Eu^{2+} is replaced with nonmagnetic Sr^{2+}, the antiferromagnetic ordering characteristic of Eu–Eu interactions disappears and a complex, two-dimensional magnetic ordering occurs as a result of Mn–Mn spin interactions.

To investigate the Eu magnetic ordering in detail, we carried out single-crystal neutron diffraction measurements in the temperature range from 1.4 K to 25 K. We searched for a variety of types of magnetic peaks, including half-integral in h, k and integral in l, integral in h, k and half-integral in l, half-integral in all indices, as well as the possibility of magnetic contributions that coincide with the nuclear Bragg peaks. No significant change in any of the nuclear reflections was observed, eliminating the possibility of a number of possible magnetic structures as well as any significant ferromagnetic component in the ordering. The only new reflections observed were with l half-integral; a few typical peaks are shown in Fig. 5. The magnetic peaks disappear above the Neél temperature, while there is no significant change in the intensities of the nuclear peaks. The half-integral values of l indicate a very simple magnetic structure in which the spins are aligned ferromagnetically in the a–b plane; these planes are stacked antiferromagnetically along the c-axis (see Fig. 1). In addition, a qualitative

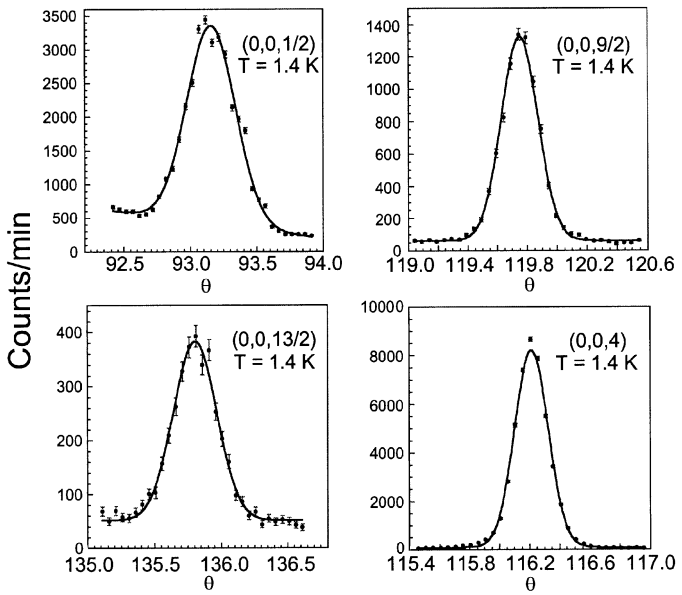

FIG. 5. Three magnetic Bragg peaks observed below the antiferromagnetic ordering temperature of 16.5 K, compared to the (0,0,4) nuclear Bragg peak.

inspection of the intensities indicates that the spins lie primarily within the a–b plane.

For a simple collinear magnetic structure, the magnetic Bragg intensities are given by

$$I_{\mathrm{M}}(\tau) = C\left(\frac{\gamma e^2}{2mc^2}\right)^2 A(\theta_B)|F_{\mathrm{M}}(\tau)|^2 \ , \qquad [1]$$

where I_{M} is the integrated intensity for the magnetic Bragg reflection located at the reciprocal lattice vector τ, the neutron–electron coupling constant in parenthesis is -0.27×10^{-12} cm, C is an instrumental constant, and $A(\theta_{\mathrm{B}})$ is an angular factor which depends on the method of measurement (sample angular rotation, θ:2θ scan, etc.) and absorption correction. The square of the magnetic structure factor is

$$|F_{\mathrm{M}}(\tau)|^2 = \langle 1-(\hat{\tau}\cdot\hat{\eta})^2\rangle\langle\mu^z\rangle^2 f^2(\tau)e^{-2W_j}\left|\sum_j \eta_j e^{i\tau\cdot r_j}\right|^2, \quad [2]$$

where $\hat{\tau}$ is a unit vector in the direction of the reciprocal lattice vector τ, $\hat{\eta}$ denotes the direction of the ordered moment of the jth ion located at $\boldsymbol{r}_j$ in the unit cell, W_j is the Debye–Waller factor, and the sum is over all magnetic atoms in the unit cell. The form factor $f(\tau)$ is the Fourier transform of the magnetization density, $\langle\mu_j^z\rangle$ is the average value of the ordered moment, and the orientation factor $\langle 1-(\hat{\tau}\cdot\hat{\eta})^2\rangle$ represents an average over all possible domains. The scattering can be put on an absolute scale by comparison with the nuclear Bragg intensities I_{N} given by

$$I_{\mathrm{N}}(\tau) = CM_\tau A(\theta_B)|F_{\mathrm{N}}(\tau)|^2, \qquad [3]$$

with

$$|F_{\mathrm{N}}(\tau)|^2 = \left|\sum_j b_j e^{-W_j} e^{i\tau\cdot r_j}\right|^2. \qquad [4]$$

Here b_j is the coherent nuclear scattering amplitude and the sum is over all atoms in the unit cell. The nuclear structure is known and F_{N} can be calculated, and we used the nuclear intensities to determine $A(\theta_B)$ empirically, which then established the relative intensities of the magnetic peaks and the absolute value of the ordered magnetic moment. Seventeen independent magnetic peaks were measured, and the intensities are in good agreement with the simple magnetic structure shown in Fig. 1, using the calculated Eu magnetic form factor (33). The Eu^{2+} spins lie in the a–b plane and are ferromagnetically coupled, while the nearest-neighbor spins along the c-axis are coupled antiferromagnetically. The ordered magnetic moment we obtained is $6.98 \pm 0.35\ \mu_{\mathrm{B}}$, where we have increased the error above the statistical uncertainty to reflect the uncertainties in our empirical determination of $A(\theta_B)$. This is in excellent agreement with the expected value of $gJ = 7\ \mu_{\mathrm{B}}$.

The temperature dependence of the magnetic intensity is shown in Fig. 6. These data were obtained by measuring at the peak maximum while varying the temperature. Complete scans were also obtained at 1.4, 5, 10, 12.5, and 15 K to determine that there was no significant broadening of the peak, as well as at 25 K to measure the (flat) background. The intensity decreases monotonically with increasing temperature, and no difference is observed on warming and cooling. Equations [1] and [2] indicate that the magnetic intensity is proportional to the square of the ordered moment $\mu^z(T)$, and the $\mu^z(T)$ obtained from these data, which is the sublattice magnetization, is shown in the lower part of the figure. The solid curve is a fit to a (mean-field) Brillouin function, which for this large a spin should provide a reasonable description of the data. We obtain a Néel temperature of 16.5 ± 0.25 K from the fit. We see, though, that there are substantial deviations from the curve, and the origin of this behavior is not known. We do not believe, however, that these deviations originate from possible coupling to the Mn spins, since this would tend to smear the phase transition, whereas here the transition is sharp (34). Possible magnetic ordering of the Mn spins will be investigated separately.

Finally, the resistivity data for $EuMn_2P_2$ in Fig. 7 indicate that it exhibits semiconducting behavior between 300 K and 120 K, at which point the resistivity became too large to measure with an electrometer. The activation

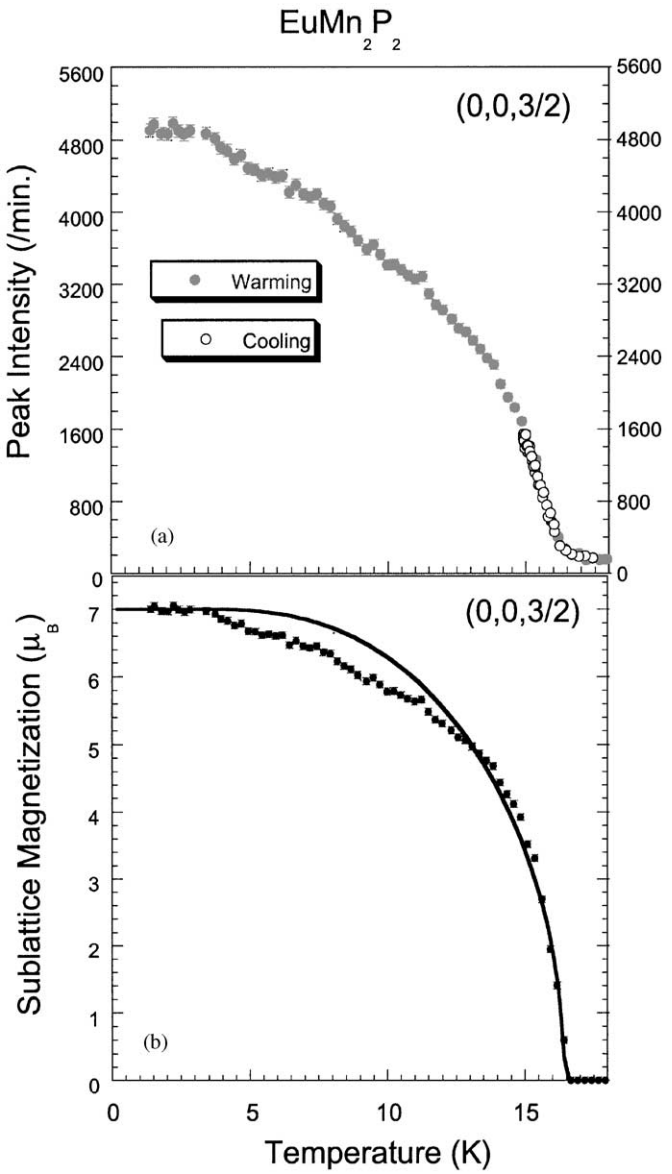

FIG. 6. (a) Temperature dependence of the intensity of the $(0,0,\frac{3}{2})$ antiferromagnetic peak as a function of temperature, indicating a sharp magnetic phase transition at 16.5 K. (b) Temperature dependence of the normalized sublattice magnetization as a function of temperature, obtained from the intensity measurements. The solid curve is a fit to a mean field theory, where we see substantial deviations between the data and the fit.

energy obtained from the fit between 120 K and 300 K is 0.0389(1) eV.

SUMMARY

Large single crystals of $EuMn_2P_2$ were grown in a Sn flux. The structure was determined by X-ray crystallography. Although compounds with 1:2:2 stoichiometry are known to exist in either the $ThCr_2Si_2$ or $CaAl_2Si_2$ structure

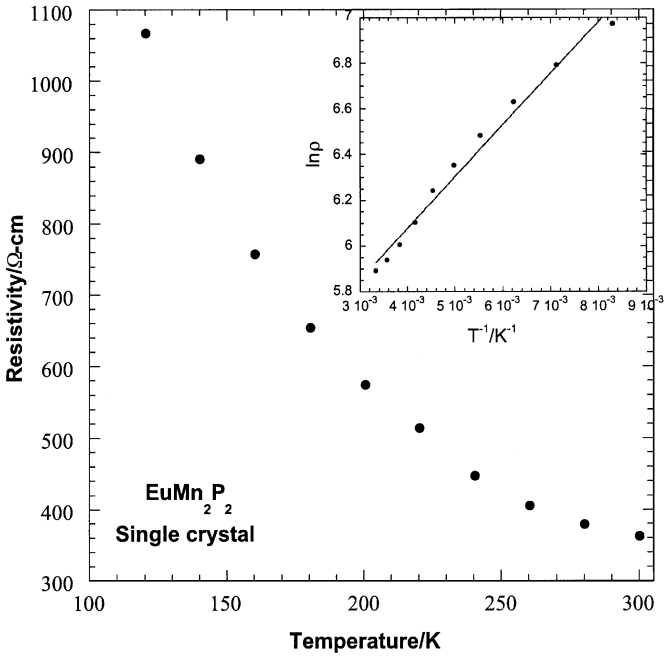

FIG. 7. $EuMn_2P_2$ single-crystal resistivity measurements from 300 K to 120 K. The inset shows ln ρ as a function of inverse temperature.

type, $EuMn_2P_2$ crystallizes in the $CaAl_2Si_2$ structure type, isostructural with $SrMn_2P_2$. $EuMn_2P_2$ is an antiferromagnetic semiconductor with a Eu Neél temperature of 16.5 K. The magnetic structure consists of ferromagnetic sheets of spins in the *a*–*b* plane which are coupled antiferromagnetically along the *c*-axis.

ACKNOWLEDGMENTS

The identification of any commercial product or trade name does not imply endorsement or recommendation by the National Institute of Standards and Technology. This research was funded by the National Science Foundation (DMR-9803074). We are indebted to Robert N. Shelton for use of the magnetometer and Peter Klavins for technical assistance.

REFERENCES

1. P. C. Canfield and Z. Fisk, *Philos. Mag. B* **65,** 1117 (1992).
2. Z. Fisk and J. P. Remeika, *in* "Growth of Single Crystals from Molten Metal Fluxes" (K. A. Gschneidner and L. Eyring, Eds.), p. 53. Elsevier Science Publishers B.V., Amsterdam, 1989.
3. V. N. Gurin and M. M. Korsukova, *Prog. Cryst. Growth Charact.* **6,** 59 (1983).
4. J. Hulliger, *Angew. Chem., Int. Ed. Engl.* **33,** 143 (1994).
5. T. Lundström, *J. Less-Common Met.* **100,** 215 (1984).
6. N. P. Luzhnaya, *J. Cryst. Growth* **3,4,** 97 (1968).
7. J. Y. Chan and S. M. Kauzlarich, *Chem. Mater.* **9,** 531 (1997).
8. S. A. Sunshine, D. Kang, and J. A. Ibers, *J. Am. Chem. Soc.* **109,** 6202 (1987).
9. M. G. Kanatzidis and A. C. Sutorik, *Prog. Inorg. Chem.* **43,** 151 (1995).

10. X. Z. Chen, S. Sportouch, B. Sieve, P. Brazis, C. R. Kannewurf, J. A. Cowen, R. Patschke, and M. G. Kanatzidis, *Chem. Mater.* **10,** 3202 (1998).
11. M. G. Kanatzidis, *Curr. Opin. Solid State Mater. Sci.* **2,** 139 (1997).
12. H. Kim, C. L. Condron, A. P. Holm, and S. M. Kauzlarich, *J. Am. Chem. Soc.* **122,** 10720 (2000).
13. H. Kim, M. M. Olmstead, J. Y. Chan, P. C. Canfield, I. R. Fisher, R. W. Henning, A. J. Schultz, and S. M. Kauzlarich, *J. Solid State Chem.* **157,** 225 (2001).
14. A. C. Payne, M. M. Olmstead, S. M. Kauzlarich, and D. J. Webb, *Chem. Mater.* **13,** 1398 (2001).
15. R. Rühl and W. Jeitschko, *Mater. Res. Bull.* **14,** 513 (1979).
16. A. Mewis, *Z. Naturforsch.* **33b,** 606 (1978).
17. S. L. Brock, J. E. Greedan, and S. M. Kauzlarich, *J. Solid State Chem.* **109,** 416 (1994).
18. S. L. Brock, J. E. Greedan, and S. M. Kauzlarich, *J. Solid State Chem.* **113,** 303 (1994).
19. D. C. Palmer, *Crystaldiffrac Professional edition*, P.O. Box 183, Bicester, Oxfordshire, OX26 3TA, UK, 2000.
20. G. M. Sheldrick, *SADABS*, Bruker AXS Inc., Madison, WI, 2000.
21. G. M. Sheldrick, *SHELXTL*, 5.10, Bruker AXS Inc., Madison, WI, 1997.
22. A. C. Payne, E. Sprauve, M. M. Olmstead, and S. M. Kauzlarich, submitted.
23. P. Klüfers and A. Mewis, *Naturforsch. Teil B* **32,** 753 (1977).
24. P. Klüfers, H. Neumann, A. Mewis, and H.-U. Schuster, *Z. Naturforsch.* **35b,** 1317 (1980).
25. P. Klüfers and A. Mewis, *Z. Kristallogr.* **169,** 135 (1984).
26. A. Artmann and A. Mewis, *Z. Anorg. Allg. Chem.* **622,** 679 (1996).
27. C. Kranenberg, D. Johrendt, A. Mewis, R. Pöttgen, G. Kotzyba, C. Rosenhahn, and B. D. Mosel, *Solid State Sci.* **2,** 215 (2000).
28. J. K. Burdett and G. J. Miller, *Chem. Mater.* **2,** 12 (1989).
29. R. Ramirez, R. Nesper, and H. G. von Schnering, *Z. Naturforsch.* **42b,** 670 (1987).
30. C. Zheng, R. Hoffmann, R. Nesper, and H. G. von Schnering, *J. Am. Chem. Soc.* **108,** 1876 (1986).
31. C. Zheng and R. Hoffmann, *J. Solid State Chem.* **72,** 58 (1988).
32. G. E. Bacon, "Neutron Diffraction." Oxford Univ. Press, Oxford, 1975.
33. M. Blume, A. J. Freeman, and R. E. Watson, *J. Chem. Phys.* **37,** 1245 (1962).
34. See, for example: J. W. Lynn, S. Skanthakumar, I. W. Sumarlin, W.-H. Li, R. N. Shelton, J. L. Peng, Z. Fisk, and S.-W. Cheong, *Phys. Rev. B* **41,** 2569 (1990); J. W. Lynn, B. Keimer, C. Ulrich, C. Bernhard, and J. L. Tallon, *Phys. Rev. B* **61,** R14964 (2000).